




Gas sloshing and cold fronts in pre-merging galaxy cluster Abell 98

ARNAB SARKAR ^{1,2,3} SCOTT RANDALL ² YUANYUAN SU,¹ GABRIELLA E. ALVAREZ ² CRAIG L. SARAZIN,⁴
CHRISTINE JONES,² ELIZABETH BLANTON,⁵ PAUL NULSEN,^{2,6} PRIYANKA CHAKRABORTY,² ESRA BULBUL,⁷ JOHN ZUHONE,²
FELIPE ANDRADE-SANTOS,² AND RYAN E. JOHNSON⁸

¹University of Kentucky, 505 Rose street, Lexington, KY 40506, USA

²Center for Astrophysics | Harvard & Smithsonian, Cambridge, MA 02138, USA

³Kavli Institute for Astrophysics and Space Research, Massachusetts Institute of Technology, 77 Massachusetts Ave, Cambridge, MA 02139, USA, Cambridge, MA 02138, USA

⁴University of Virginia, Charlottesville, VA 22904, USA

⁵Boston University, Boston, MA 02215, USA

⁶ICRAR, University of Western Australia, 35 Stirling Hwy, Crawley, WA 6009, Australia

⁷Max Planck Institute for Extraterrestrial Physics, Giessenbachstrasse 1, 85748 Garching, Germany

⁸Gettysburg College, Gettysburg, PA 17325, USA

ABSTRACT

We present deep *Chandra* observations of the pre-merger galaxy cluster Abell 98. Abell 98 is a complex merging system. While the northern (A98N) and central subclusters (A98S) are merging along the north-south direction, A98S is undergoing a separate late-stage merger, with two distinct X-ray cores. We report detection of gas sloshing spirals in A98N and in the eastern core of A98S. We detect two cold front edges in A98N. We find two more surface brightness edges along the east direction of the eastern core and west direction of the western core of A98S. We measure the temperatures and gas densities across those edges, and find that the eastern edge appears to be a cold front while the western edge is a shock front with a Mach number of $\mathcal{M} \approx 1.5$. We detect a “tail” of X-ray emission associated with the eastern core of A98S. Our measurement indicates that the tail is cooler than the surrounding gas at a $4.2\text{-}\sigma$ level, suggesting the tail is part of a cool core remnant that has been ram-pressure stripped.

Keywords: X-rays: galaxies: clusters – galaxies: clusters: intracluster medium

1. INTRODUCTION

Abell 98 (hereafter A98) is an early-stage merger (Forman et al. 1981) with three main sub-clusters, A98S (central), A98N (northern), and A98SS (southern). Previous studies have reported a shock front associated with the northern sub-cluster and a filament connecting the northern and central sub-clusters. (e.g., Alvarez et al. 2022; Sarkar et al. 2022). Alvarez et al. (2022) also reported a filament extending to the north beyond A98N, indicating A98N and A98S lie along a large-scale cosmic filament. In this work, we focus on the northern and central subclusters.

Cluster mergers along large scale filaments leave imprints on the intra-cluster medium (ICM) in the form of

shocks, cold fronts, and gas sloshing spirals (e.g., Markevitch et al. 2001, 2002; Ascasibar & Markevitch 2006; Markevitch & Vikhlinin 2007). Numerical simulations show that when a subhalo passes the density peak of the central cluster with a nonzero impact parameter, it accelerates the DM and gas peaks towards it. At first, they travel together, but as the gas peak moves through the surrounding gas, the ICM velocity field around the main cluster core decelerates the gas peak due to the ram pressure, resulting in a separation between the DM and gas peaks. While the DM peak continues moving towards the receding subhalo, the gas peak is held back. During the core passage, the direction of this motion rapidly changes, leading to an abrupt change in the ram-pressure force exerted on the gas peak, which then overshoots the potential minimum. Eventually, the gas peak turns around and starts sloshing back and forth around the DM peak. This sloshing motion can be in-

ferred from imaging studies, which reveal the presence of sharp discontinuities in the surface brightness and temperature. In these features, the brighter (denser) side of the surface brightness jump is colder than the fainter (less dense) side; hence this is a “cold front”, as opposed to the shock front (e.g., Markevitch et al. 2000; Vikhlinin et al. 2001).

Gas sloshing motion can induce multiple cold fronts at different radii, growing over time and combining into a spiral pattern, known as a “gas sloshing” spiral (e.g., Ascasibar & Markevitch 2006; Markevitch & Vikhlinin 2007; Roediger et al. 2011). These spiral structures are commonly observed in several galaxy clusters, such as A1763 (Douglass et al. 2018), A2029 (Paterno-Mahler et al. 2013), A2052 (Blanton et al. 2011), and the Fornax cluster (Su et al. 2017). Measurements of gas properties across the cold fronts reveal that the gas pressure stays almost the same across these cold fronts, as observed in several galaxy clusters, e.g., A2029 (Clarke et al. 2004), Perseus (Ichinohe et al. 2019), A2142 (Rossetti et al. 2013), and in galaxy groups (Gastaldello et al. 2013). This limits the relative gas motion, as ram pressure forces would increase the gas pressure inside of the cold front. Though there is pressure equilibrium across the cold fronts, observations of other clusters show that the gas outside the edge is nearly at hydrostatic equilibrium, but the gas inside the edge is not (e.g., Fabian et al. 2001; Markevitch & Vikhlinin 2007).

A98 is an early-stage merger at a redshift of $z \approx 0.1042$ (Paterno-Mahler et al. 2014). Previous observations confirm that this is a system of Bautz-Morgan type II-III and richness of class 3 (Abell et al. 1989). The central sub-cluster A98S is at a redshift of $z \approx 0.1063$ and hosts a wide-angle tail (WAT) radio source (4C 20.04; O’Donoghue et al. 1993). The other two sub-clusters, A98N ($z \approx 0.1043$) and A98SS ($z \approx 0.1218$), are at projected distances of ~ 1.1 Mpc north and 1.4 Mpc south from the central sub-cluster, respectively. (e.g., Jones & Forman 1999; Burns et al. 1994). A98N is a cool core cluster with an asymmetric warmer gas arc in the south (Paterno-Mahler et al. 2014). In paper I (Sarkar et al. 2022), we investigated this scenario in detail. We reported a shock front with a Mach number of $\mathcal{M} \approx 2.3$ at about 420 kpc south from the A98N core.

The primary goals of this paper are to map the thermodynamic structure and reveal any sub-structures associated with the central regions of A98N and A98S. We investigate the surface brightness edges near A98N and A98S and measure gas properties across them. We organize the paper as follows: in Section 2, we describe the data reduction procedures; in Section 3, we analyse the actual, residual, the Gaussian Gradient Magni-

Table 1. *Chandra* observation log

Obs ID	Obs Date (J2000)	Exp. time (ks)	PI
11876	2009 Sep 17	19.2	S. Murray
11877	2009 Sep 17	17.9	S. Murray
21534	2018 Sep 28	29.5	S. Randall
21535	2019 Feb 19	24.7	S. Randall
21856	2018 Sep 26	30.5	S. Randall
21857	2018 Sep 30	30.6	S. Randall
21880	2018 Oct 09	9.9	S. Randall
21893	2018 Nov 11	17.9	S. Randall
21894	2018 Nov 14	17.8	S. Randall
21895	2018 Nov 14	28.6	S. Randall

tude (GGM) images, and report the surface brightness profiles and electron density jumps; in Section 4, we show results from the spectral analysis, including the gas properties profiles; finally, in Section 5 we discuss and summarize our results.

Throughout this paper, we adopt a cosmology of $H_0 = 70 \text{ km s}^{-1} \text{ Mpc}^{-1}$, $\Omega_\Lambda = 0.7$, and $\Omega_m = 0.3$. Unless otherwise stated, all reported error bars correspond to a 90% confidence level.

2. DATA PREPARATION

Abell 98 was observed with *Chandra* during two epochs, once in September 2009 for 37 ks split into two observations and later in September 2018 – February 2019 for 190 ks divided into eight observations. The combined exposure time is ~ 227 ks (detailed observation logs are listed in Table 1). We performed the *Chandra* data reduction with CIAO version 4.12 and CALDB version 4.9.4 distributed by the Chandra X-ray Center (CXC). We have followed a standard data analyzing thread [§].

All level 1 event files were reprocessed using the `chandra_repro` task by employing the latest gain, charge transfer inefficiency correction, and filtering out the bad grades. VFAINT mode was used to improve the background screening. Light curves were extracted and filtered using the `lc_clean` script to identify and remove periods affected by flares. The filtered exposure times are listed in Table 1. We used the `reproject_obs` task to

[§] <http://cxc.harvard.edu/ciao/threads/index.html>

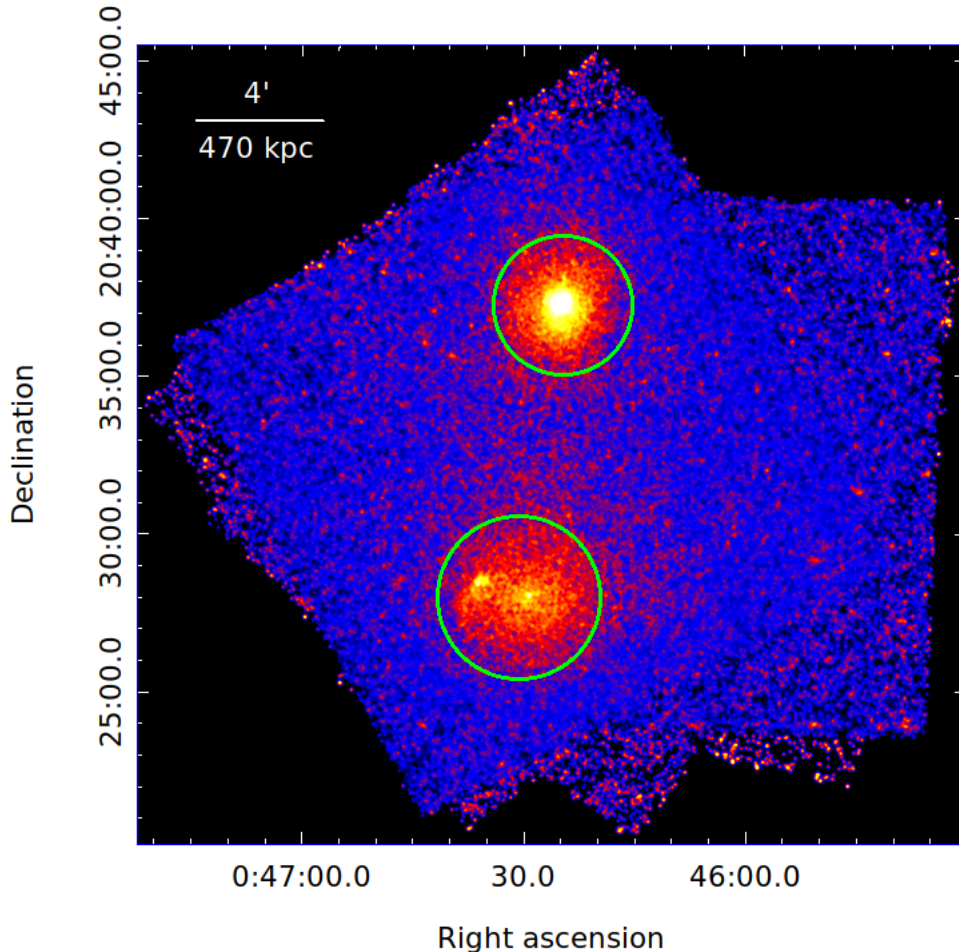


Figure 1. Merged, exposure corrected, and background subtracted *Chandra* ACIS-I image of northern (A98N) and central (A98S) sub-clusters of A98 in the 0.5–2.0 energy band. The image has been smoothed with a $\sigma=2''$ Gaussian kernel. The dual structure of A98S is clearly visible. Green circles represent the regions used for the measurement of global ICM properties of both sub-clusters.

reproject all observations to a common tangent position and combine them. The exposure maps in the 0.5–2.0 keV energy bands were created using the `flux_obs` script by providing a weighting spectrum, which was generated using the `make_instmap_weights` task with an absorbed APEC plasma emission model and a plasma temperature of 3 keV. To remove the underexposed edges of the detector, we set the pixel value to zero for those pixels with an exposure of less than 15% of the combined exposure time.

Point sources were identified using `wavdetect` with a range of wavelet radii between 1–16 pixels. We set the detection threshold to $\sim 10^{-6}$, which guaranteed $\lesssim 1$ spurious source detection per CCD. We used `blanksky` background observations to model the non-X-ray background, emission from foreground structures (e.g., Galactic Halo and Local Hot Bubble) along the observed direction and unresolved faint background sources. The `blanksky` background files were generated

using the `blanksky` task and then reprojected to match the coordinates of the observations. We finally normalized the resulting `blanksky` background to match the 9.5–12 keV count rates in our observations.

3. IMAGING ANALYSIS

Figure 1 shows a slightly smoothed image of A98N (northern sub-cluster) and A98S (central sub-cluster) in the 0.5–2 keV band, obtained after co-adding all ten observations and by applying the correction for exposure non-uniformity. As reported by earlier studies, the cluster is an early-stage merger, with the merger axis likely aligned along a local N-S large-scale filament connecting A98N and A98S (e.g., Paterno-Mahler et al. 2014; Alvarez et al. 2022; Sarkar et al. 2022).

3.1. A98N

We used a residual image of A98N to search for any faint substructures, e.g., associated with gas sloshing

or merger shocks. The residual image was created by subtracting the azimuthally averaged surface brightness at each radius (centered on A98N), as shown in Figure 2. The residual image shows an apparent surface brightness excess spiraling clockwise (if traced inward from large radius), a classic signature of gas sloshing, and is brightest to the north/north-east of the cluster center. The farthest visible arc of the spiral extends out to 140 kpc south from the cluster center. Similar gas sloshing spirals have also been observed in other galaxy clusters, e.g., A2029 (Paterno-Mahler et al. 2013), Perseus (Fabian et al. 2011), A1763 (Douglass et al. 2018), A2319 (Ichinohe et al. 2021), and A2142 (Roediger et al. 2012).

The sloshing spiral in A98N indicates A98N experienced a separate merger, un-associated with the ongoing early-stage merger between A98N and A98S, probably in the past few Gyr, based on the timescale for the formation of the sloshing spirals seen in simulations (ZuHone et al. 2010). Spiral patterns are understood to have formed when a cool-core system experiences an infall of a subcluster with a non-zero impact parameter. Simulations of the formation of spiral patterns show that during the formation process, the relative velocity between the gas density and dark matter peak stays below 400 km/s (Ascasibar & Markevitch 2006), and the average offset between gas density-dark matter peaks is below 30 kpc (Johnson et al. 2010). Additionally, the winding direction of a spiral (when traced inward from large radii) reveals the infalling subcluster’s trajectory, since the direction of angular momentum of spiraling-in gas is the same as that of the infalling subcluster (ZuHone et al. 2011; Douglass et al. 2018). The clockwise winding spiral pattern seen in A98N indicates that the perturbing subcluster may have passed the A98N core from the west to the north-east on the southern side.

Next, to reveal any substructures and associated sharp features in the A98N core, we obtained a GGM filtered image of A98N with a filtering length scale of 8 pixels. Each pixel is $0.492'' \times 0.492''$. Figure 2 (right) shows the GGM image of the A98N core. We observe two regions with relatively large surface brightness gradients in the core, peaking at ~ 60 kpc to the north and 70 kpc to the east of the A98N core (indicated by the white arrows in Figure 2), sharply declining at larger radii. To determine the significance of these apparent features, we extracted surface brightness profiles in the east and north directions in 90° sectors. The energy band is restricted to 0.5-2 keV to minimize the effect of variation of X-ray emissivity with temperature while maximizing the signal-to-noise ratio. We match the centers of the

curvature of the surface brightness edges to the center of the sectors. Figure 3 shows the extracted surface brightness profiles in the east and north directions.

Both surface brightness profiles exhibit discontinuities and overall shapes that are consistent with what is expected from a projected spherical density discontinuity (Markevitch et al. 2000). We fit each profile with a broken power-law model

$$n(r) \propto \begin{cases} r^{-\alpha_1}, & \text{if } r < r_{edge} \\ \frac{1}{jump} r^{-\alpha_2}, & \text{if } r \geq r_{edge} \end{cases} \quad (1)$$

where $n(r)$, r_{edge} , and $jump$ represent 3D electron density at a radius r , the radius of the putative edge, and the density jump factor, respectively. α_1 and α_2 are the slopes inside and outside the edge, respectively. We project the estimated emission measure profile onto the sky plane and fit the observed surface brightness profile by varying the slopes, edge radius, and the magnitude of the jump (similar to what we did for the shock front in paper I; Sarkar et al. 2022). Figure 3 displays the best-fit models (red) and the 3D density profiles (inset) for both directions. For the east direction, we obtain best-fit power-law indices of $\alpha_1 = 0.70 \pm 0.01$ and $\alpha_2 = 1.0 \pm 0.01$. The associated density jump across the edge is $\rho_2/\rho_1 = 1.38 \pm 0.03$, where suffix 2 and 1 represent the regions inside and outside of the edge, respectively. Similarly, for the north direction, we find a best-fit power-law index of $\alpha_1 = 0.80 \pm 0.03$ and $\alpha_2 = 1.10 \pm 0.03$ with a corresponding density jump of 1.47 ± 0.01 . We obtain the best-fit edge radius of 70 ± 6 kpc for the east edge and 60 ± 4 kpc for the north edge, as measured with respect to the centroid of the central X-ray surface brightness peak. Both edge radii are consistent with the position of the steep gradients seen in the GGM image (Figure 2). We estimate the uncertainty of each parameter by allowing all the other model parameters to vary freely.

3.2. A98S

Figure 1 reveals that the central sub-cluster (A98S) hosts two distinct surface brightness peaks. Paterno-Mahler et al. (2014) showed that the western peak coincides with a WAT AGN. Using the SDSS-r magnitude of the galaxy distribution of A98, they concluded that these two surface brightness peaks are likely to be associated with two BGCs from two merging subclusters. We denote the western sub-cluster as A98Sa and the eastern sub-cluster as A98Sb. Figure 1 exhibits that the X-ray emission is extended from east to west and appears to cut off abruptly northeast of the A98Sb. To better highlight these features, we create an unsharp-mask image in the following way. We smoothed the background

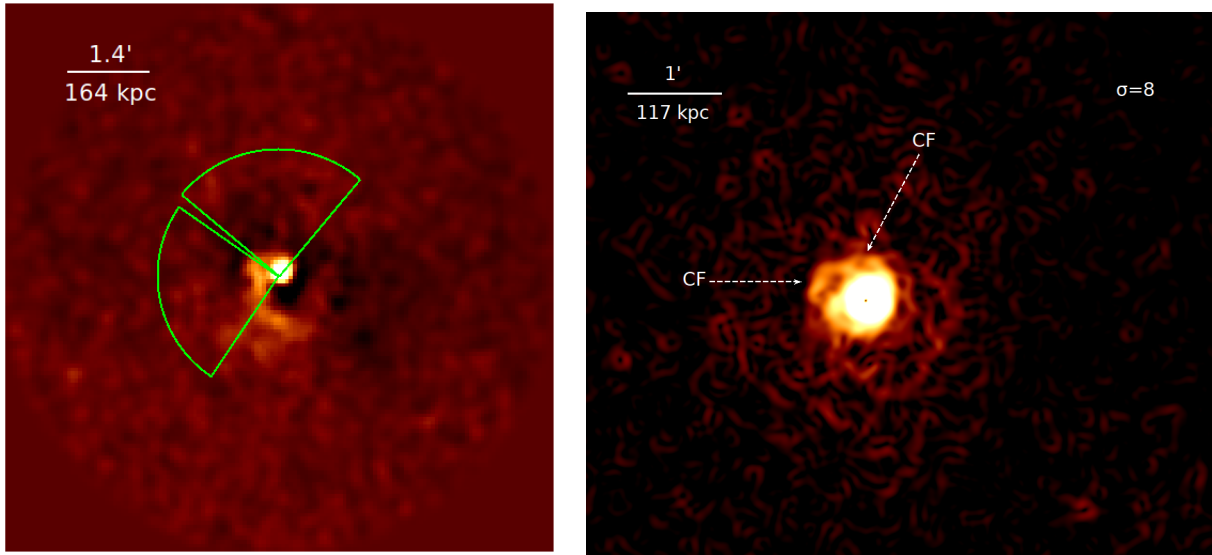


Figure 2. *Left:* Residual image of A98N in the 0.5-2 keV energy band obtained after subtracting the azimuthal averaged surface brightness profile from Figure 1. The image has been smoothed with a $1.5''$ Gaussian kernel. A spiral pattern can clearly be seen travelling clock-wise if traced inward. Green sectors are used for spectral analysis. *Right:* Gaussian gradient magnitude filtered image of A98N smoothed by $\sigma = 8$ pixels and each pixel = $0.492''$. The north and east cold fronts are marked by white arrows.

subtracted and exposure corrected X-ray image by 2D Gaussian kernels with $\sigma = 2''$ and $20''$. The images are then subtracted to obtain the unsharp-masked image, as shown in Figure 4 (left). The unsharp-masked image features the different substructures in the ICM of A98S. A98S appears to be separated into three concentrations of X-ray emitting gas: the two sub-cluster cores (A98Sa and A98Sb) and a “tail” of emission to the southeast originating from the central region of A98Sb. The unsharp-masked image also reveals a surface brightness edge northeast of A98Sb. In contrast, A98Sa shows a relatively uniform morphology with no prominent surface brightness edges.

We next examine the surface brightness edge seen in the northeast of A98Sb by extracting a surface brightness profile across the edge, as shown in Figure 5 (right). The surface brightness profile shows a discontinuity similar to what we have seen in A98N. We fit the profile with a broken power-law model, as detailed in Section 3.1. Figure 5 displays the best-fit model (in red) and 3D density profile (inset). We obtain a best-fit power-law index of $\alpha_1 = 0.650 \pm 0.003$ and $\alpha_2 = 0.7 \pm 0.1$. The associated density jump across the edge is $\rho_2/\rho_1 = 2.8 \pm 0.2$ with a best-fit edge radius of 28 ± 2 kpc.

To further investigate any faint substructure associated with both sub-cluster cores (A98Sa and A98Sb), we obtain a β -model subtracted image of A98S. We use two 2D elliptical β -models centered at both sub-cluster cores to fit the surface brightness image in the 0.5-2 keV energy band. We also include a constant in the model to

account for the sky background and any residual particle background. The model is fitted in *Sherpa*, and the best-fit parameters are obtained by minimizing the Cash statistic (Cash 1979). The best-fit 2D β -model image is then subtracted from the source image of A98S, leaving the residual image shown in Figure 6.

Figure 6 reveals a spiral structure likely to be associated with the gas sloshing resulting from a recent fly-by of a subhalo near the central region of A98Sb. The excess emission from the “tail” seen in the residual and unsharp-masked image may suggest a trail of materials that has been ram pressure stripped in the gravitational potential. Alternatively, the spiral structure and the tail may be due to ram pressure stripping, as the subcluster orbits in the main cluster’s potential, and the tail is potentially influenced by ICM “weather” (e.g. bulk turbulence). Either scenario could be true. A further deeper observation is required to probe the feature in detail.

Compared to A98Sb, A98Sa shows a relatively regular morphology. Since there are clear radio lobes, one might expect cavities in the ICM evacuated by these lobes (Mathews & Brighenti 2008). A weak detection of cavities at the location of the lobes was reported in Paterno-Mahler et al. (2014). We therefore extract an azimuthal surface brightness profile, shown in Figure 5, centering at the A98Sa core with a radius of $\sim 150''$. The sharp increase in the surface brightness to the east with a peak at $\sim 165^\circ$ is due to the surface brightness peak associated with A98Sb. Similar results were ob-

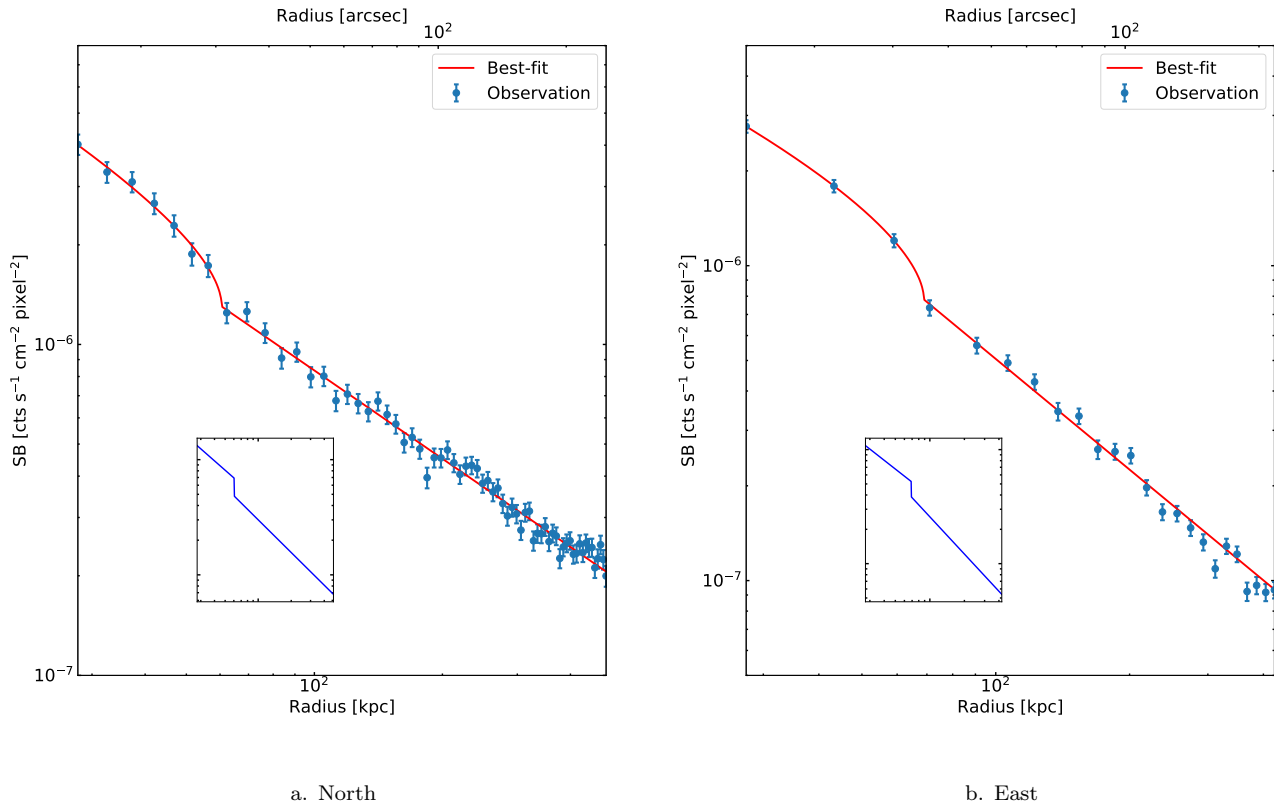


Figure 3. *Left:* Northern sector surface brightness profile of A98N in the 0.5 - 2 keV energy band fitted with a broken power-law model. The best-fit deprojected density profile is shown in inset figure. All error bars are at $1\text{-}\sigma$ level. *Right:* similar to the *left* figure, but for eastern sector.

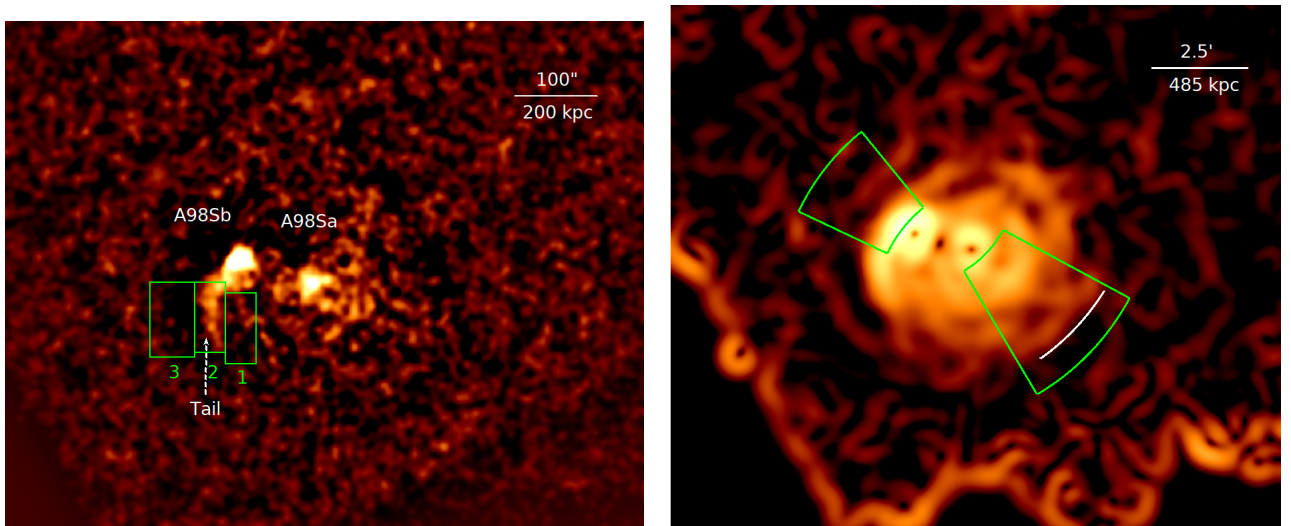


Figure 4. *Left:* Unsharp-masked image of A98Sa and A98Sb created by subtracting images smoothed by 2D Gaussians with $\sigma = 2''$ and $20''$. Green regions are used for the spectral analysis. The 'tail' is marked with white arrow. *Right:* Gaussian gradient magnitude filtered image of A98S. The image is smoothed by $\sigma = 13''$. A sharp gradient is clearly visible to southwest of the A98Sa and marked by a white curve. Green sectors are used for spectral analysis.

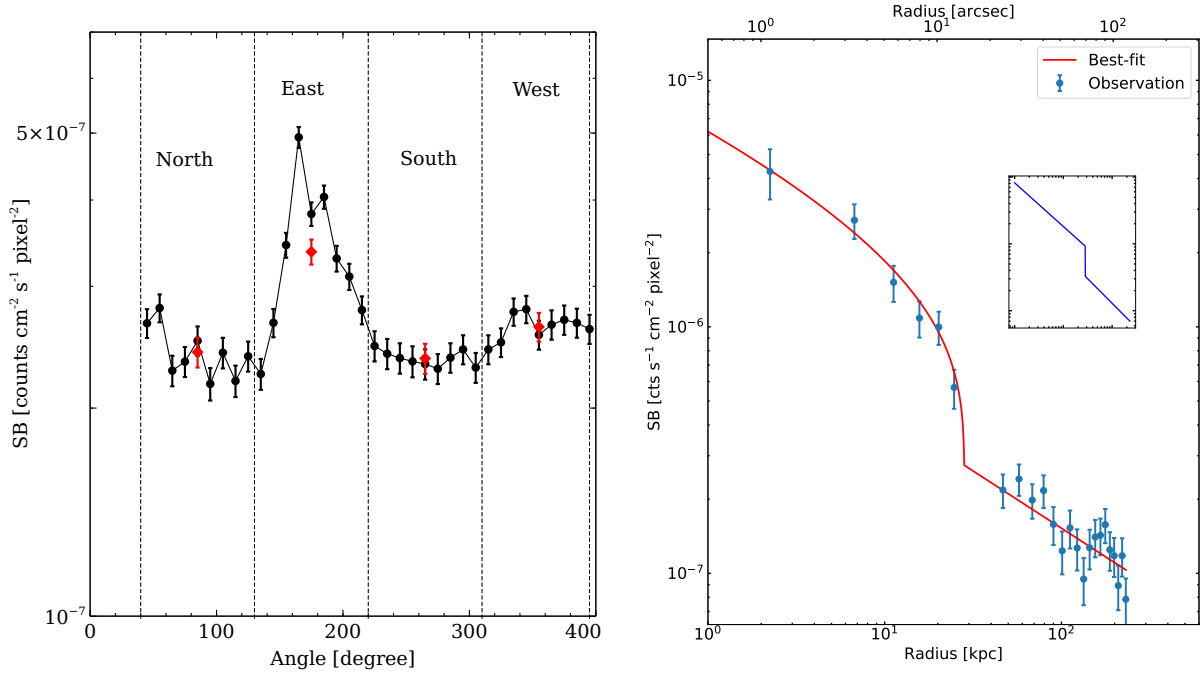


Figure 5. *Left:* Azimuthal surface brightness profile in the 0.5 - 2 keV energy band centered on the A98Sa core. Black represents the surface brightness at individual angles and red represents the binned surface brightness in 90° sectors. The north and south sectors contain the northern and southern lobe of the WAT. East sector contains the second BCG, A98Sb. *Right:* Eastern sector (as shown in Figure 4) surface brightness profile of A98Sb in the 0.5 - 2 keV energy band fitted with a broken power-law model. Deprojected density profile is shown in inset figure.

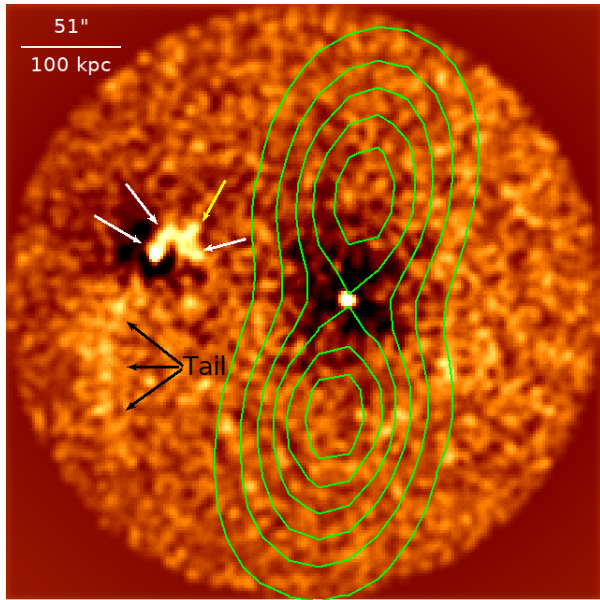


Figure 6. Residual image of excess X-ray emission of A98Sa and A98Sb with 1.4 GHz radio contours overlaid in green. The image was created by subtracting two 2D elliptical β -models from an unbinned image with point sources excluded. White, yellow, black arrows indicate the spiral structure, the bifurcation of spiral pattern, and the ‘tail’ of X-ray emission, respectively.

tained by Paterno-Mahler et al. (2014). However, we do not find any significant difference between the surface brightness in any other directions. Since A98Sa hosts a WAT radio source, the absence of any substantial decrement in the surface brightness at north and south directions indicates that either the radio lobes are filled with X-ray emitting gas, or the jet axis is far enough from the plan of the sky to prevent a detection. Several previous studies also found jets and lobes in other merging galaxy clusters, such as A2199 (Nulsen et al. 2013), A1682 (Clarke et al. 2019), A1446 (Douglass et al. 2008), A562 (Douglass et al. 2011; Gómez & Calderón 2020), and A1775 (Hu et al. 2021).

The GGM image of A98S shown in Figure 4 features a possible surface brightness edge at about 370 kpc southwest of A98Sa. We extract a surface brightness profile across the edge and fit that profile using a broken power-law model, as seen in Figure 10. We obtain best-fit power-law indices of $\alpha_1 = 0.7 \pm 0.1$ and $\alpha_2 = 0.9 \pm 0.2$. The electron density jumps by a factor of 1.7 ± 0.5 across the edge. We find the best-fit edge radius of 375 ± 10 kpc coincides with the apparent rapid change in the surface brightness gradient seen in GGM image (Figure 4). We discuss the spectral properties of the surface brightness edges seen in A98Sa and A98Sb in Section 4.4.

4. SPECTRAL ANALYSIS

4.1. Global ICM properties

To constrain the global properties of both sub-clusters, we first extracted spectra from two circular regions centering on each sub-cluster core with a radius of $\sim 2'$ for A98N and $3'$ for A98S (roughly similar regions as seen in Paterno-Mahler et al. 2014). Both regions contain $\gtrsim 32000$ background-subtracted counts in the 0.6-7 keV energy band and contain a vast majority of the cluster emission after eliminating the point sources, which is imperative to probe the global properties of both sub-clusters. The background spectra were hard-band scaled (10–12 keV) and subtracted from the source spectra before fitting. We restricted the spectral fitting to the 0.6-7 keV energy band and binned the spectra to contain a minimum of 40 counts per bin. We fixed the redshift to $z = 0.1042$. The spectral analysis was performed using Xspec version 12.11.1. All resolved point sources were excluded before the spectral analysis. We used solar abundance table given in Asplund et al. (2009). For each sub-cluster, a single-temperature fit to the observed spectra using an absorbed thermal plasma emission model (i.e. `phabs` \times `apec`) produced a good fit (Smith et al. 2001).

For A98N, we measured a temperature of 3.05 ± 0.09 keV and a metal abundance of $0.63 \pm 0.10 Z_{\odot}$ with a χ^2/dof of 786/761. Additionally, spectral fitting to the central sub-cluster (A98S) yielded a best-fit temperature of 3.04 ± 0.12 keV and an abundance of $0.42 \pm 0.10 Z_{\odot}$ with a χ^2/dof of 870/886. In both cases, the hydrogen column density was fixed to the Galactic value, $N_H = 3.06 \times 10^{20} \text{ cm}^{-2}$, estimated using the LAB survey (Kalberla et al. 2005). Paterno-Mahler et al. (2014) also reported the temperature and abundance of both sub-clusters using a 38 ks *Chandra* observation and a 37 ks *XMM-Newton* observation. For both sub-clusters, our results better determine the gas temperatures and abundances, but are consistent with the earlier measurement by Paterno-Mahler et al. (2014).

4.2. Temperature map

For understanding the thermodynamic structures of the ICM in A98N and A98S, we constructed a temperature map following the techniques described in Randall et al. (2008, 2009). We extracted an elliptical region containing both sub-clusters and binned the image with 10 background-subtracted counts per pixel to aid the computational speed. For each pixel, we extracted spectra from a circular region with a radius set such that the region contains ~ 2300 background-subtracted source counts in the 0.6-7 keV energy band. This particular number of source counts was adopted to ensure that the

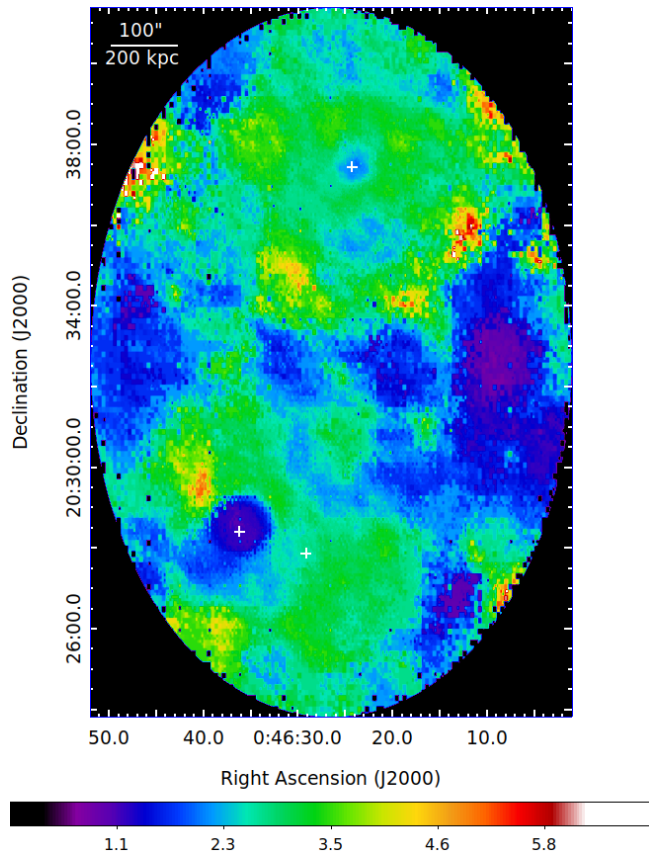


Figure 7. Projected temperature map of A98N/A98S. Units are in keV. The individual sub-cluster centers are marked by white crosses. A98N is at RA = 0:46:25.0, Dec = 20:38:00, A98Sa is at RA = 0:46:35.0, Dec = 20:28:03, and A98Sb is at RA = 0:46:28.0, Dec = 20:28:00. The warmer gas ‘arc’ can be seen to the south of A98N. A98N and A98Sb have cool central cores, whereas A98Sa has a warmer, roughly isothermal core.

uncertainty in temperature measurements in the fainter regions of the ICM was $\lesssim 25\%$. We generated appropriate response and ancillary response files for each region, and the background spectra were subtracted from the total spectra.

Figure 7 shows the temperature map of A98N/A98S. A98N and A98Sb appear to have cool cores with hot gas enclosing them, which is expected for cool core clusters. In contrast, A98Sa appears to have a warm core with a uniform gas temperature of ~ 3.7 keV within 20 kpc of the core. This suggests that A98a was transformed into a non cool-core cluster during an earlier subcluster merger.

The northern sub-cluster has an asymmetric ‘arc’ of hot gas with a temperature of > 3.5 keV, which is clearly visible in Figure 7. This arc radius (~ 400 kpc) is consis-

tent with the radius of the shock front that we reported in paper I (Sarkar et al. 2022), suggesting the ‘arc’ consists of shock heated gas. The uncertainties in the temperature map range from $\lesssim 15\%$ for brighter regions and are between 20-25% for the fainter regions. Since each region in the temperature map contains a fixed source count, the extraction regions are larger in the fainter parts of the ICM, making the temperature map highly smoothed.

4.3. A98N: East and North cold fronts

We extracted spectra from the eastern and northern sectors in A98N to measure the temperature and density changes across the surface brightness edges seen in Figure 3. Each sector was divided into five individual bins. These bins were positioned to measure the gas properties on either side of the surface brightness edges while maintaining a minimum of 3000 source counts in each extracted spectrum. We set this lower limit to guarantee enough photon counts for good spectral fitting and constraints on the parameters. Spectra were extracted from those bins in each sector.

We fixed the metallicity to an average value of $0.4 Z_{\odot}$ since it was poorly constrained if left free (Russell et al. 2010). The best-fit parameters were obtained by minimizing the Cash statistics. Figure 8 shows the radial profiles of the best-fit projected temperatures and pressures obtained across the eastern and northern edges. The temperature of the gas increases from the A98N core to the larger radii in both directions. Our measurements confirm the electron density jumps detected in the surface brightness profile analysis, but the temperature and pressure profiles appear continuous across the edges. However, the cooler gas inside of the edges is more consistent with a cold front interpretation. Similar cold fronts are also found in other clusters such as the Bullet cluster (Markevitch et al. 2002), A2142 (Markevitch et al. 2000), A3667 (Vikhlinin et al. 2001), A2146 (Russell et al. 2010), A2256 (Ge et al. 2020), A2554 (Erdim & Hudaverdi 2019), Perseus (Walker et al. 2017, 2020), and in many others (Botteon et al. 2018).

4.4. A98S: cold front, tail, and western SB edge

A98S consists of two individual sub-clusters, A98Sa and A98Sb. The temperature map in Figure 7 shows that the central region of A98Sb is cooler than A98Sa. Previous *Chandra* observations by Paterno-Mahler et al. (2014) showed that A98Sb is cooler than A98Sa at a $3\text{-}\sigma$ level. With our deeper *Chandra* observations, we examined the spectra of each sub-cluster to measure the global ICM temperatures of individual sub-clusters. We extracted spectra from a circular region with $50''$ radius and centering at both sub-clusters cores. These

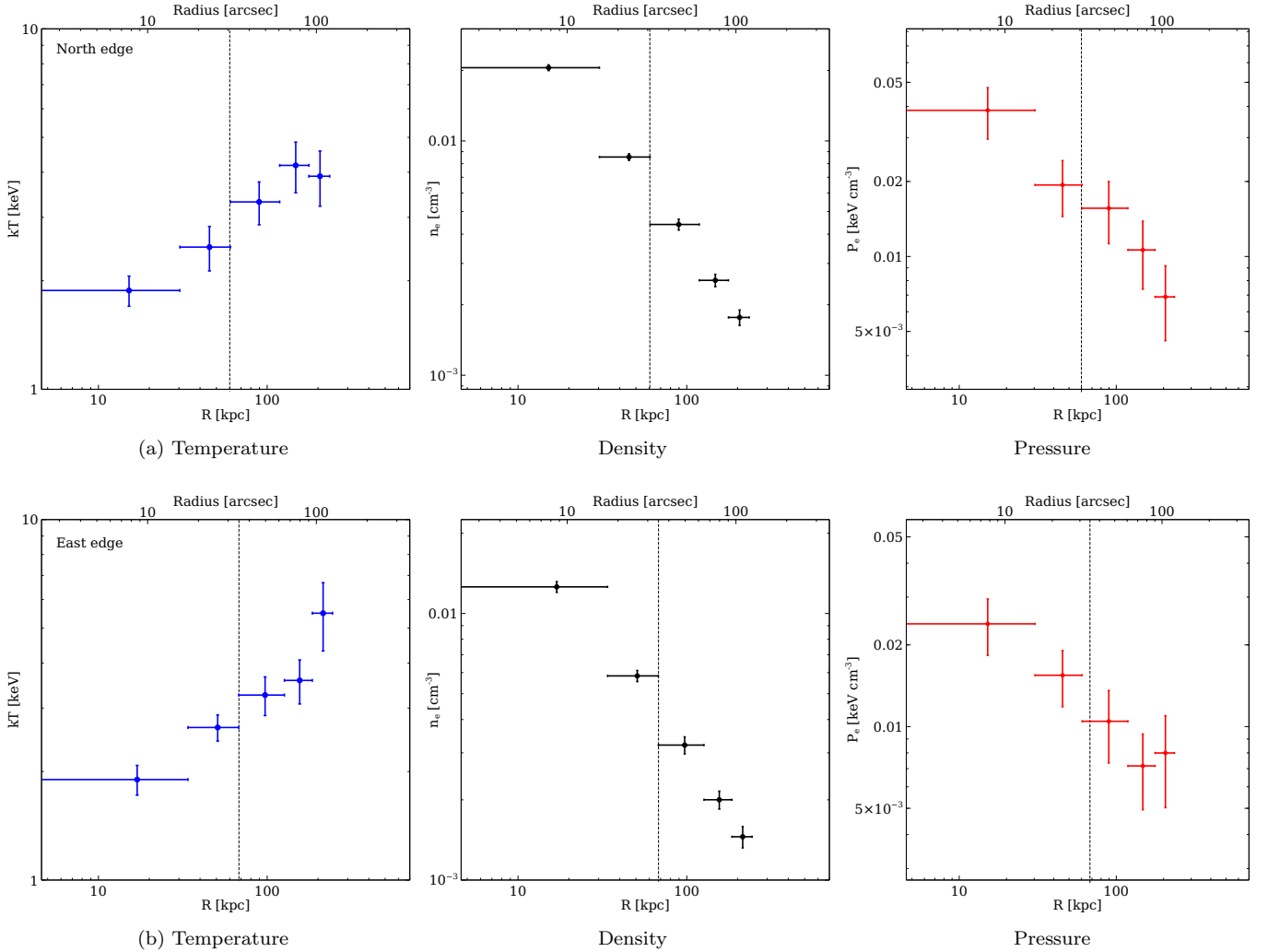


Figure 8. *Top panel:* Northern sector projected temperature, deprojected electron density, and projected electron pressure profiles centered on the A98N core. The metallicity was fixed to $0.4 Z_{\odot}$. The projected pressure profile was estimated using the deprojected densities and projected temperatures. The vertical dashed line represents the position of the surface brightness edges. *Bottom panel:* similar as above but for eastern sector.

regions were chosen based on the peaks of the X-ray emission, assuming each of them includes the prominent extended emission from the corresponding sub-cluster. Point sources and background spectra were analyzed as described in Section 4. We measured a temperature of $3.70^{+0.33}_{-0.28}$ keV for the western sub-cluster (A98Sa) and $2.47^{+0.21}_{-0.20}$ for the eastern sub-cluster (A98Sb). Our measured temperatures are consistent with that of Paterno-Mahler et al. (2014) within their uncertainties (90% confidence limit). We also found that the A98Sb is cooler than the A98Sa at a $5\text{-}\sigma$ level. This implies that A98Sb has a remnant cool core, whereas the core of A98Sa has been disrupted, so that this is a non cool-core cluster. Since A98Sa hosts a WAT radio source (4C 20.04; O’Donoghue et al. 1993), the surrounding ICM may be heated by AGN jets. Similar ICM heat-

ing through AGN feedback is also found in other galaxy clusters such as A2052 (Blanton et al. 2011), Perseus (Fabian et al. 2003), A2626 (Ignesti et al. 2018, 2020), and A1795 (Kokotanekov et al. 2018). Alternatively, the core of A98Sa may have been disrupted by either the ongoing merger or a previous merger.

We next examined the “tail” like substructure of the eastern sub-cluster that appeared in the unsharp masked image (Figure 4). We extracted spectra from three individual regions, as shown in Figure 4. For region 2, this yielded a temperature of $kT = 1.8^{+0.3}_{-0.2}$ keV and an abundance of $Z = 0.35^{+0.49}_{-0.24} Z_{\odot}$. Due to low photon counts in regions 1 and 3, we linked the parameters for those two regions while fitting, assuming they have similar temperature and abundance. For regions 1 and 3 together, we measured a temperature of $kT = 3.1^{+0.6}_{-0.4}$

keV and an abundance of $Z = 0.80_{-0.57}^{+1.01} Z_{\odot}$. We found the tail is significantly cooler than the surrounding gas at about $4.2\text{-}\sigma$ level, which suggests that it is likely to be a cool-core remnant that is being ram pressure stripped.

Figure 5 shows that A98Sb has a surface brightness edge in the northeast direction at about 28 kpc from its core. To measure the temperature across the surface brightness edge, we divided the eastern sector into four individual regions and extracted spectra from them. Those regions were drawn to contain a minimum of 1000 background-subtracted photon counts in each extracted spectrum. We set this lower limit to ensure reasonable constraints on the parameters. We fitted each spectrum with the abundance fixed to $Z = 0.4 Z_{\odot}$. Figure 9 shows the best-fit projected temperature profile of the eastern sector. The projected temperature of the gas increases rapidly at about 28 kpc, by a factor of ~ 3.6 . This temperature jump coincides with the surface brightness edge at 28 kpc, as shown in Figure 9, and corresponds to a drop in the deprojected electron density by a factor of ~ 2.8 . Figure 9 also shows the projected electron pressure profile of the eastern sector. We found that the electron pressure is roughly constant across the surface brightness edge. We, therefore, confirm this edge as a cold front contact discontinuity.

We next examined the surface brightness edge shown in Figure 10 (left) southwest of A98Sa by extracting spectra from that sector dividing it into five individual regions. We fitted the spectrum from each region with the abundance fixed to $0.4 Z_{\odot}$. The best-fit projected temperature profiles are shown in Figure 10 (right) with different levels of uncertainty. Considering both levels of uncertainties, we found that the temperature profile rises to $kT = 5.1$ keV at about ~ 375 kpc, then drops suddenly to $kT = 3.3$ keV with a jump factor of ~ 1.5 . Taken all together, this is consistent with a shock. From the 3D density jump factor we obtained a Mach number of the shock to be $\mathcal{M} \approx 1.5$, consistent with the Mach number estimated from the temperature jump. Similar Mach numbers from measurements bolster the likelihood that the surface brightness edge is due to a shock front.

5. SUMMARY

We have presented results from deep 227 ks *Chandra* observations of an early-stage merger A98N/A98S. Our analysis indicates that the cluster is experiencing a complex merger. While the northern sub-cluster (A98N) and southern sub-cluster (A98S) are merging along the N-S, the two sub-clusters of A98S (A98Sa and A98Sb) are undergoing a later-stage merger in the E-W direction. We summarize our findings below -

- The residual image of A98N shown in Figure 2 reveals a gas sloshing spiral winding clockwise when traced inward from a large radius. The sloshing spiral in A98N indicates that it too experienced a separate merger, probably in the past few Gyr based on the timescale for the formation of the sloshing spirals seen in simulations.
- We have detected two cold fronts in the north and east directions at about 60 kpc and 70 kpc, respectively, from the A98N core. For the northern cold front, we obtain a drop in the deprojected electron density by a factor of $\rho_2/\rho_1 \approx 1.47 \pm 0.01$. This jump corresponds to an increase in the projected temperature by a factor of 1.4. Similarly, for the eastern cold front, we find a decrease in the electron density by a factor of $\rho_2/\rho_1 \approx 1.38 \pm 0.03$ and an increment in the temperature by a factor of 1.3. These two cold fronts are likely to be associated with the gas sloshing at the central region of A98N.
- With our deeper *Chandra* data, we find the average temperature of the A98Sa, $kT = 3.70_{-0.28}^{+0.33}$ keV and of the A98Sb, $kT = 2.47_{-0.20}^{+0.21}$ keV, consistent with that of Paterno-Mahler et al. (2014). We report that the eastern sub-cluster is cooler than the western sub-cluster with about a $5\text{-}\sigma$ significance.
- Figure 6 shows the excess X-ray emission near the central region of A98Sb appears to be a spiral pattern winding counter-clockwise if traced inward from a larger radius. The spiral structure is more likely to be associated with the gas sloshing at the central region of A98Sb, which a recent merger may trigger. We have detected a cold front in the east direction of A98Sb associated with the gas sloshing spiral. We measure a drop in the deprojected electron density by a factor of $\rho_2/\rho_1 \approx 2.8 \pm 0.02$ and a rise in the projected gas temperature by a factor of 3.6 across the front.
- The unsharp-masked image shown in Figure 4 exhibits a tail of X-ray emission in the south/southwest direction of the A98Sb core. Our measurement shows that the tail is considerably cooler ($1.8_{-0.2}^{+0.3}$ keV) than the surrounding gas ($3.1_{-0.4}^{+0.6}$ keV) at a $4.2\text{-}\sigma$ level and the A98Sb core ($2.47_{-0.20}^{+0.21}$ keV) at a $2.9\text{-}\sigma$ level. This implies that the tail is likely to be ram pressure stripped material from a cool-core remnant.
- We have reported detecting a surface brightness edge at 375 kpc southwest from the A98Sa core

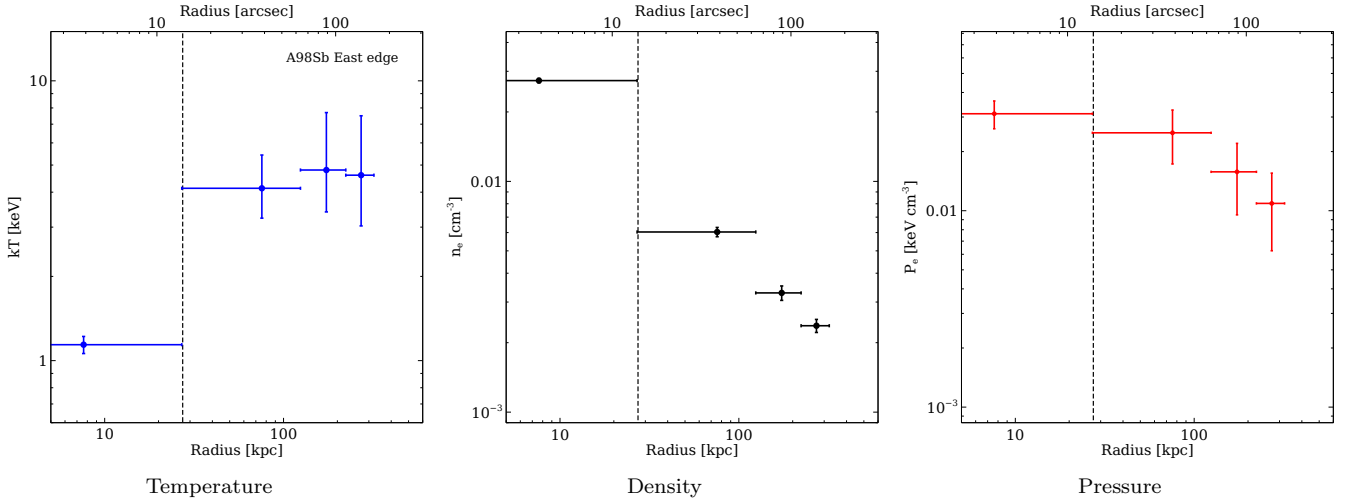


Figure 9. Eastern sector projected temperature, deprojected electron density, and projected electron pressure profiles centered on the A98Sb core. The metallicity was fixed to $0.4 Z_{\odot}$. The projected pressure profile was estimated using the deprojected densities and projected temperatures. Vertical dashed line represents the position of the surface brightness edge.

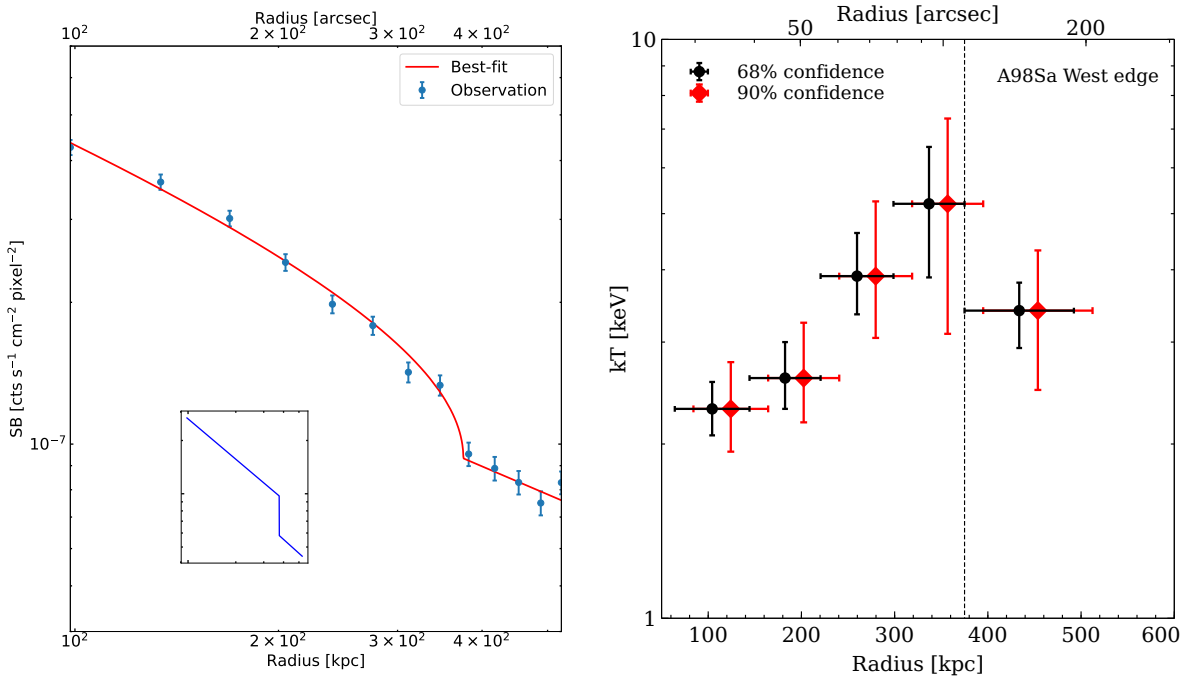


Figure 10. *Left:* western sector surface brightness profile of A98Sa in the 0.5-2 keV energy band fitted with a broken power-law model. Deprojected density profile is shown in inset figure. *Right:* western sector projected temperature profiles of A98Sa. Black and red represent the uncertainties estimated with 68% and 90% confidence level, respectively. The red data points are shifted to the right for the purpose of clarity and comparison. Vertical dashed line represents the position of the surface brightness edge.

visible in Figure 10. The deprojected electron density drops by a factor of $\rho_2/\rho_1 \approx 1.7 \pm 0.5$ and the projected temperature drops by a factor of ≈ 1.5 , suggesting the edge is a shock front with a Mach number of $\mathcal{M} \approx 1.5$.

1 This work is based on observations obtained with
2 *Chandra* observatory, a NASA mission. AS and SR
3 are supported by the grant from NASA’s *Chandra*
4 X-ray Observatory, grant number GO9-20112X. CLS
5 was supported in part by NASA *XMM-Newton* grant
6 80NSSC22K1510 and *Chandra* grant GO1-22120X.

REFERENCES

- Abell, G. O., Corwin, Harold G., J., & Olowin, R. P. 1989, *ApJS*, 70, 1, doi: [10.1086/191333](https://doi.org/10.1086/191333)
- Alvarez, G. E., Randall, S. W., Su, Y., et al. 2022, *ApJ*, 938, 51, doi: [10.3847/1538-4357/ac91d3](https://doi.org/10.3847/1538-4357/ac91d3)
- Ascasibar, Y., & Markevitch, M. 2006, *ApJ*, 650, 102, doi: [10.1086/506508](https://doi.org/10.1086/506508)
- Asplund, M., Grevesse, N., Sauval, A. J., & Scott, P. 2009, *ARA&A*, 47, 481, doi: [10.1146/annurev.astro.46.060407.145222](https://doi.org/10.1146/annurev.astro.46.060407.145222)
- Blanton, E. L., Randall, S. W., Clarke, T. E., et al. 2011, *ApJ*, 737, 99, doi: [10.1088/0004-637X/737/2/99](https://doi.org/10.1088/0004-637X/737/2/99)
- Botteon, A., Gastaldello, F., & Brunetti, G. 2018, *MNRAS*, 476, 5591, doi: [10.1093/mnras/sty598](https://doi.org/10.1093/mnras/sty598)
- Burns, J. O., Rhee, G., Owen, F. N., & Pinkney, J. 1994, *ApJ*, 423, 94, doi: [10.1086/173792](https://doi.org/10.1086/173792)
- Cash, W. 1979, *ApJ*, 228, 939, doi: [10.1086/156922](https://doi.org/10.1086/156922)
- Clarke, A. O., Scaife, A. M. M., Shimwell, T., et al. 2019, *A&A*, 627, A176, doi: [10.1051/0004-6361/201935584](https://doi.org/10.1051/0004-6361/201935584)
- Clarke, T. E., Blanton, E. L., & Sarazin, C. L. 2004, *ApJ*, 616, 178, doi: [10.1086/424911](https://doi.org/10.1086/424911)
- Douglass, E. M., Blanton, E. L., Clarke, T. E., Randall, S. W., & Wing, J. D. 2011, *ApJ*, 743, 199, doi: [10.1088/0004-637X/743/2/199](https://doi.org/10.1088/0004-637X/743/2/199)
- Douglass, E. M., Blanton, E. L., Clarke, T. E., Sarazin, C. L., & Wise, M. 2008, *ApJ*, 673, 763, doi: [10.1086/523886](https://doi.org/10.1086/523886)
- Douglass, E. M., Blanton, E. L., Randall, S. W., et al. 2018, *ApJ*, 868, 121, doi: [10.3847/1538-4357/aae9e7](https://doi.org/10.3847/1538-4357/aae9e7)
- Erdim, M. K., & Hudaverdi, M. 2019, *MNRAS*, 488, 2917, doi: [10.1093/mnras/stz1912](https://doi.org/10.1093/mnras/stz1912)
- Fabian, A. C., Sanders, J. S., Allen, S. W., et al. 2003, *MNRAS*, 344, L43, doi: [10.1046/j.1365-8711.2003.06902.x](https://doi.org/10.1046/j.1365-8711.2003.06902.x)
- Fabian, A. C., Sanders, J. S., Ettori, S., et al. 2001, *MNRAS*, 321, L33, doi: [10.1046/j.1365-8711.2001.04243.x](https://doi.org/10.1046/j.1365-8711.2001.04243.x)
- Fabian, A. C., Sanders, J. S., Allen, S. W., et al. 2011, *MNRAS*, 418, 2154, doi: [10.1111/j.1365-2966.2011.19402.x](https://doi.org/10.1111/j.1365-2966.2011.19402.x)
- Forman, W., Bechtold, J., Blair, W., et al. 1981, *ApJL*, 243, L133, doi: [10.1086/183459](https://doi.org/10.1086/183459)
- Gastaldello, F., Di Gesu, L., Ghizzardi, S., et al. 2013, *ApJ*, 770, 56, doi: [10.1088/0004-637X/770/1/56](https://doi.org/10.1088/0004-637X/770/1/56)
- Ge, C., Liu, R.-Y., Sun, M., et al. 2020, *MNRAS*, 497, 4704, doi: [10.1093/mnras/staa2320](https://doi.org/10.1093/mnras/staa2320)
- Gómez, P. L., & Calderón, D. 2020, *AJ*, 160, 152, doi: [10.3847/1538-3881/aba831](https://doi.org/10.3847/1538-3881/aba831)
- Hu, D., Xu, H., Zhu, Z., et al. 2021, *ApJ*, 913, 8, doi: [10.3847/1538-4357/abf09e](https://doi.org/10.3847/1538-4357/abf09e)
- Ichinohe, Y., Simionescu, A., Werner, N., Fabian, A. C., & Takahashi, T. 2019, *MNRAS*, 483, 1744, doi: [10.1093/mnras/sty3257](https://doi.org/10.1093/mnras/sty3257)
- Ichinohe, Y., Simionescu, A., Werner, N., Markevitch, M., & Wang, Q. H. S. 2021, *MNRAS*, 504, 2800, doi: [10.1093/mnras/stab1060](https://doi.org/10.1093/mnras/stab1060)
- Ignesti, A., Gitti, M., Brunetti, G., et al. 2018, *A&A*, 610, A89, doi: [10.1051/0004-6361/201731380](https://doi.org/10.1051/0004-6361/201731380)
- Ignesti, A., Shimwell, T., Brunetti, G., et al. 2020, *A&A*, 643, A172, doi: [10.1051/0004-6361/202039056](https://doi.org/10.1051/0004-6361/202039056)
- Johnson, R. E., Markevitch, M., Wegner, G. A., Jones, C., & Forman, W. R. 2010, *ApJ*, 710, 1776, doi: [10.1088/0004-637X/710/2/1776](https://doi.org/10.1088/0004-637X/710/2/1776)
- Jones, C., & Forman, W. 1999, *ApJ*, 511, 65, doi: [10.1086/306646](https://doi.org/10.1086/306646)
- Kalberla, P. M. W., Burton, W. B., Hartmann, D., et al. 2005, *A&A*, 440, 775, doi: [10.1051/0004-6361:20041864](https://doi.org/10.1051/0004-6361:20041864)
- Kokotanekov, G., Wise, M. W., de Vries, M., & Intema, H. T. 2018, *A&A*, 618, A152, doi: [10.1051/0004-6361/201833222](https://doi.org/10.1051/0004-6361/201833222)
- Markevitch, M., Gonzalez, A. H., David, L., et al. 2002, *ApJL*, 567, L27, doi: [10.1086/339619](https://doi.org/10.1086/339619)
- Markevitch, M., & Vikhlinin, A. 2007, *PhR*, 443, 1, doi: [10.1016/j.physrep.2007.01.001](https://doi.org/10.1016/j.physrep.2007.01.001)
- Markevitch, M., Vikhlinin, A., & Mazzotta, P. 2001, *ApJL*, 562, L153, doi: [10.1086/337973](https://doi.org/10.1086/337973)
- Markevitch, M., Ponman, T. J., Nulsen, P. E. J., et al. 2000, *ApJ*, 541, 542, doi: [10.1086/309470](https://doi.org/10.1086/309470)
- Mathews, W. G., & Brighenti, F. 2008, *ApJ*, 685, 128, doi: [10.1086/590402](https://doi.org/10.1086/590402)
- Nulsen, P. E. J., Li, Z., Forman, W. R., et al. 2013, *ApJ*, 775, 117, doi: [10.1088/0004-637X/775/2/117](https://doi.org/10.1088/0004-637X/775/2/117)

- O'Donoghue, A. A., Eilek, J. A., & Owen, F. N. 1993, *ApJ*, 408, 428, doi: [10.1086/172600](https://doi.org/10.1086/172600)
- Paterno-Mahler, R., Blanton, E. L., Randall, S. W., & Clarke, T. E. 2013, *ApJ*, 773, 114, doi: [10.1088/0004-637X/773/2/114](https://doi.org/10.1088/0004-637X/773/2/114)
- Paterno-Mahler, R., Randall, S. W., Bulbul, E., et al. 2014, *ApJ*, 791, 104, doi: [10.1088/0004-637X/791/2/104](https://doi.org/10.1088/0004-637X/791/2/104)
- Randall, S., Nulsen, P., Forman, W. R., et al. 2008, *ApJ*, 688, 208, doi: [10.1086/592324](https://doi.org/10.1086/592324)
- Randall, S. W., Jones, C., Kraft, R., Forman, W. R., & O'Sullivan, E. 2009, *ApJ*, 696, 1431, doi: [10.1088/0004-637X/696/2/1431](https://doi.org/10.1088/0004-637X/696/2/1431)
- Roediger, E., Brüggén, M., Simionescu, A., et al. 2011, *MNRAS*, 413, 2057, doi: [10.1111/j.1365-2966.2011.18279.x](https://doi.org/10.1111/j.1365-2966.2011.18279.x)
- Roediger, E., Lovisari, L., Dupke, R., et al. 2012, *MNRAS*, 420, 3632, doi: [10.1111/j.1365-2966.2011.20287.x](https://doi.org/10.1111/j.1365-2966.2011.20287.x)
- Rossetti, M., Eckert, D., De Grandi, S., et al. 2013, *A&A*, 556, A44, doi: [10.1051/0004-6361/201321319](https://doi.org/10.1051/0004-6361/201321319)
- Russell, H. R., Sanders, J. S., Fabian, A. C., et al. 2010, *MNRAS*, 406, 1721, doi: [10.1111/j.1365-2966.2010.16822.x](https://doi.org/10.1111/j.1365-2966.2010.16822.x)
- Sarkar, A., Randall, S., Su, Y., et al. 2022, *ApJL*, 935, L23, doi: [10.3847/2041-8213/ac86d4](https://doi.org/10.3847/2041-8213/ac86d4)
- Smith, R. K., Brickhouse, N. S., Liedahl, D. A., & Raymond, J. C. 2001, *ApJL*, 556, L91, doi: [10.1086/322992](https://doi.org/10.1086/322992)
- Su, Y., Nulsen, P. E. J., Kraft, R. P., et al. 2017, *ApJ*, 851, 69, doi: [10.3847/1538-4357/aa989e](https://doi.org/10.3847/1538-4357/aa989e)
- Vikhlinin, A., Markevitch, M., & Murray, S. S. 2001, *ApJ*, 551, 160, doi: [10.1086/320078](https://doi.org/10.1086/320078)
- Walker, S. A., Hlavacek-Larrondo, J., Gendron-Marsolais, M., et al. 2017, *MNRAS*, 468, 2506, doi: [10.1093/mnras/stx640](https://doi.org/10.1093/mnras/stx640)
- Walker, S. A., Mirakhor, M. S., ZuHone, J., et al. 2020, arXiv e-prints, arXiv:2006.14043, <https://arxiv.org/abs/2006.14043>
- ZuHone, J. A., Markevitch, M., & Johnson, R. E. 2010, *ApJ*, 717, 908, doi: [10.1088/0004-637X/717/2/908](https://doi.org/10.1088/0004-637X/717/2/908)
- ZuHone, J. A., Markevitch, M., & Lee, D. 2011, *ApJ*, 743, 16, doi: [10.1088/0004-637X/743/1/16](https://doi.org/10.1088/0004-637X/743/1/16)